

1 **Replenishment of near-surface water ice by impacts into Ceres' volatile-rich crust:** 2 **Observations by Dawn's Gamma Ray and Neutron Detector**

3 **T. H. Prettyman¹, N. Yamashita¹, M. E. Landis², J. C. Castillo-Rogez³, N. Schörghofer¹,**
4 **C. M. Pieters^{1,4}, H. G. Sizemore¹, H. Hiesinger⁵, S. Marchi⁶, H. Y. McSween⁷, R. S. Park,³**
5 **M. J. Toplis⁸, C. A. Raymond³, C. T. Russell⁹**

6 ¹Planetary Science Institute, Tucson, AZ. ² Laboratory for Atmospheric and Space Physics,
7 University of Colorado, , Boulder, CO. ³Jet Propulsion Laboratory, California Institute of
8 Technology, Pasadena, CA. ⁴Brown University, Providence, RI. ⁵Institut für Planetologie,
9 Westfälische Wilhelms-Universität Münster, Münster, Germany. ⁶Southwest Research Institute,
10 Boulder, CO. ⁷University of Tennessee, Knoxville, TN. ⁸L'Institut de Recherche en
11 Astrophysique et Planétologie (University of Toulouse, UT3, CNRS), Toulouse, France.
12 ⁹University of California Los Angeles, Los Angeles, CA.

13 Corresponding author: Thomas Prettyman (prettyman@psi.edu)

14 **Key Points:**

- 15 • Neutron spectroscopy reveals enhanced hydrogen concentrations in the outermost
16 meter of the surface of a prominent young, complex crater
- 17 • Results confirm Ceres outer crust is ice rich and support retention of water ice within
18 impact ejecta on airless, icy bodies
- 19 • The data imply partial control of regolith ice content by large impacts, relaxing
20 constraints on surface age and regolith grain size

21 **Abstract**

22 Ceres' regolith contains water ice that has receded in response to insolation-driven sublimation.
23 Specially targeted, high spatial-resolution measurements of hydrogen by Dawn's Gamma Ray
24 and Neutron Detector reveal elevated hydrogen concentrations in and around Occator, a young,
25 90-km diameter, complex crater located at 19.82N where near-surface ice is not expected. The
26 excess hydrogen is explained by impact excavation of water-rich outer crustal materials and their
27 emplacement in the crater floor and ejecta blanket. This is supported by thermophysical models
28 that show water ice could survive at sub-meter depths, given Occator's relatively young age
29 (~20 Myr). We hypothesize that the regolith can be replenished with ice from large impacts and
30 that this process partially controls the distribution and depth of near surface ice. This is supported
31 by results from Occator and similarities in the global distribution of hydrogen and the pattern of
32 large craters (20-100 km diameter).

33 **Plain Language Summary**

34 The outermost meter of dwarf planet Ceres contains water ice that is gradually sublimating in
35 response to heating of the surface by sunlight. Since Ceres' axis of rotation is nearly
36 perpendicular to the Sun's rays, ice has receded to greater depths at the equator than the poles.
37 The distribution of subsurface ice within this outer layer was inferred from measurements of
38 hydrogen by Dawn's Gamma Ray and Neutron Detector. Special operations during Dawn's last
39 mission phase brought the spacecraft close to the surface, enabling measurements within and
40 around a large, young crater called Occator. Anomalously high concentrations of hydrogen were
41 detected, suggesting the impact that formed Occator excavated water rich materials from the
42 crust and deposited them on the surface. Comparison of the global distribution of hydrogen with
43 the pattern of large craters on Ceres further supports excavation of crustal ice by impacts as a
44 partial control on the depth of ice near the surface. Results confirm that Ceres' crust is rich in
45 water ice and show that ice can survive in materials ejected by impacts into airless, icy bodies.

46 **1 Introduction**

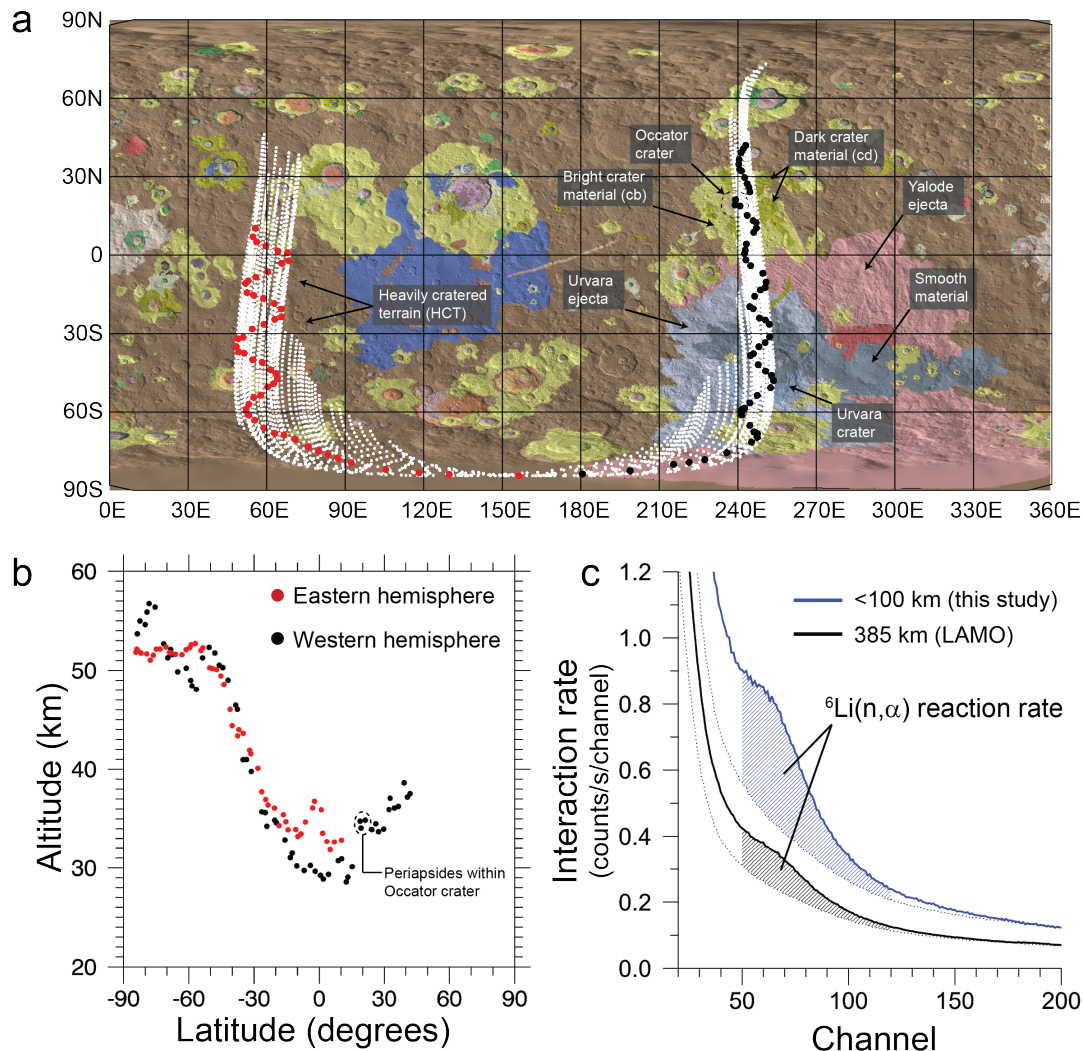
47 The dwarf planet Ceres, the largest body in the main asteroid belt (469.7-km volumetric
48 mean radius), is water rich (Russell et al., 2016). As Ceres evolved, liquid water interacted with
49 rock within the interior to produce hydrated minerals (McSween et al., 2017). Ceres' average
50 interior structure consists of a rocky mantle and a ~40-km thick crust, dominated by the frozen
51 remnants of an ancient, global ocean (Castillo-Rogez et al., 2018; Ermakov et al., 2017).
52 Rheological constraints indicate that the crust is volatile-rich, containing water ice,
53 phyllosilicates, salts, and possibly clathrate hydrates (Fu et al., 2017). Residual brines at the base
54 of the crust could be a source for active cryomagmatism (e.g., Quick et al., 2019; Raymond et al.,
55 2020; Ruesch et al., 2019). High-resolution gravity data imply a positive density gradient in
56 Ceres' crust, interpreted as enrichment of dense oceanic precipitates in the lower part of the
57 crust in contrast to a volatile-rich outer crust (Park et al., 2020).

58 The ice content of different crustal layers can be inferred from diverse remote-sensing
59 data sets, including nuclear spectroscopy, geomorphology, and gravity. Surficial water ice has
60 been detected within some mid-to-high latitude craters (Combe et al., 2019) and the presence of
61 complex craters with fluidized ejecta, lobate flow features, and pitted terrain indicate water ice is
62 abundant within the few km depths probed by impacts (e.g., Sizemore et al., 2017; 2019).

63 GRaND measurements reveal the presence of a global ice table within a few millimeters of the
64 surface at the poles that has receded to greater depths at lower latitudes due to increased solar
65 insolation, consistent with Ceres' obliquity history (Prettyman et al., 2017).

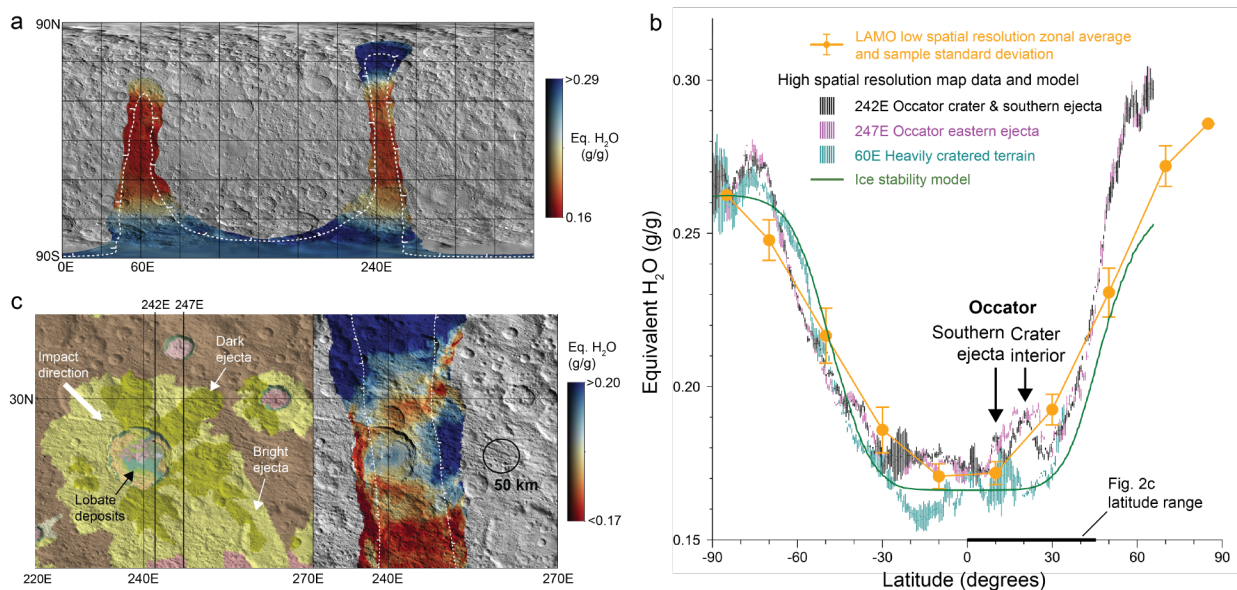
66 Previous analyses of GRaND data support 20 vol.% water ice in the near-surface ice
67 table, with ice below the depth of sensitivity (a few decimeters) near the equator; whereas, the
68 bulk crustal average water content is inferred to be about >60 vol.% based on geophysical
69 measurements of crustal density and strength (Fu et al., 2017; Park et al., 2020). Impact
70 processes are key to understanding the connection between the volatile-rich crustal reservoir and
71 the regolith. A simple-to-complex transition occurs for craters with diameters greater than about
72 10 km (Hiesinger et al., 2016; Schenk et al., 2021). Furthermore, impacts that formed large
73 craters exposed crustal materials from a wide range of depths within the outer crust, with the
74 excavation depth roughly 10% of the crater diameter (Marchi et al., 2016). As such, large
75 impacts have the potential to redistribute ice within the outer crust.

76 We use hydrogen mapping data acquired by Dawn's Gamma Ray and Neutron Detector
77 (GRaND) to investigate the effect of impacts on shallow-regolith water ice content. We
78 hypothesize that impacts can bring water ice from the outer crust to the surface, replenishing the
79 regolith with ice. As such, the distribution of near surface water ice in the upper few decimeters
80 of the regolith as sensed by GRaND is shaped both by large impacts and long-term insolation-
81 driven sublimation. We test this hypothesis with high-spatial-resolution GRaND data acquired in
82 Dawn's final mission phase. The high-resolution data are sensitive to the composition of the
83 interior and ejecta blanket of the young, complex crater Occator. Lower-resolution data acquired
84 by GRaND during Dawn's primary mission enable investigations of the global relationships
85 between cratering and regolith hydrogen content.



86

87 **Figure 1.** Close-proximity measurements. (a) Highly eccentric orbits (south-north trajectory)
 88 enabled the acquisition of GRaND data with 35s accumulation intervals at over 5000 locations
 89 with altitudes less than 100 km (white points). Circles (red and black) indicate the measurement
 90 locations closest to the periapsides of the 113 orbits used in the analysis (Text S1). The
 91 measurements sampled geologic units in the eastern and western hemispheres along the 60E and
 92 240E meridian, including the ~20 Myr old Occator crater (Neesemann et al., 2019), centered at
 93 239.33E and 19.82N, and its ejecta blanket. See Williams et al. (2019) for geological unit
 94 definitions. (b) Altitudes of periapsis less than 30 km were achieved at some locations near the
 95 equator, with higher altitudes towards the poles. (c) Close proximity enabled acquisition of
 96 neutron counting data with high spatial resolution and precision. The ${}^6\text{Li}(n,\alpha)$ reaction rate in
 97 GRaND's lithium-loaded glass (LiG) scintillator (shaded areas) is sensitive to regolith hydrogen
 98 content (Text S1). The average reaction rate below 100 km was about $3\times$ higher than observed in
 99 Dawn's low altitude mapping orbit (LAMO).



100

101 **Figure 2.** Distribution of subsurface hydrogen. **(a)** The equirectangular map of water-equivalent
 102 hydrogen, was determined from ${}^6\text{Li}(n,\alpha)$ reaction rates measured below 100 km altitude. The
 103 white contour line, which approximates the boundary of the point cloud in Fig. 1a, delineates the
 104 most highly sampled region, with contributions from >50 measurements at each map location.
 105 Outside the point cloud, hydrogen concentrations are extrapolated from the data. **(b)** The
 106 distribution of hydrogen in **(a)** is plotted for selected meridians. The population standard
 107 deviation in hydrogen concentration, determined by Monte Carlo error propagation, is
 108 represented by vertical lines. The distribution of hydrogen, which is more variable than the
 109 LAMO zonal average (Prettyman et al., 2017) is consistent with a globally receding ice table.
 110 The mapping algorithm was applied to simulated, low-altitude neutron measurements of the
 111 distribution of ice determined by thermophysical modeling (i.e., ice-cemented soil with 1 μm
 112 grain size, 0.2 porosity, and 10 wt.% water ice) (Prettyman et al., 2017). These parameters
 113 produced a close match to the neutron counting data acquired in LAMO. **(c)** The low-altitude
 114 data reveal elevated concentrations of hydrogen in and around Occator crater. Map variations on
 115 spatial scales greater than 50 km (black circle) can be interpreted as changes in subsurface
 116 composition. A geologic map of the Occator region is provided for context (Scully et al., 2019;
 117 Williams et al., 2018, with units defined therein). Map data are superimposed on shaded relief.

118 2 Hydrogen mapping with high spatial resolution GRaND data

119 In Dawn's final mission phase, the spacecraft maneuvered into a highly eccentric orbit
 120 with low periapsis (30-50 km, Figs. 1a, 1b and Text S1). This enabled acquisition of high-
 121 spatial-resolution GRaND data, on scales comparable to geologic units over a wide range of
 122 latitudes in both the eastern and western hemispheres. Analyses of high resolution data can be
 123 compared with the elemental measurements determined from GRaND data acquired in Dawn's
 124 primary mission from a low altitude mapping orbit (LAMO) with 385 km mean altitude

125 (Prettyman et al., 2017). Since spatial resolution scales with altitude (Prettyman et al., 2019), the
126 eccentric orbits achieved up to 10× improvement in spatial resolution compared to LAMO.

127 A primary target of the eccentric orbits was Occator crater, a very young (<20 Myr)
128 (Neesemann et al., 2019) 90-km diameter, complex crater located at about 19.82N and 239.33E
129 within Hanami Planum. The crater contains prominent faculae as well as lobate deposits and
130 fluidized ejecta, which likely contain water ice (Scully et al., 2019). Thus, the geomorphology
131 supports impact into an ice-rich substrate. The crater and immediate surroundings were well
132 sampled with multiple orbits with periapsides near 35-km altitude, corresponding to an intrinsic
133 spatial resolution of about 50 km full-width-at-half-maximum for GRaND. This allowed
134 measurements of hydrogen within the crater interior and portions of the ejecta blanket, providing
135 constraints on processes underlying crater formation and the fate of hydrogen-bearing materials.

136 The concentration of hydrogen was determined from the leakage flux of low-energy
137 neutrons produced by the interaction of galactic cosmic rays (GCRs) with Ceres' regolith.
138 Measurements of the ${}^6\text{Li}(n,\alpha)$ reaction rate with GRaND's +Z lithium-loaded glass (LiG)
139 scintillator (Prettyman et al., 2011) provide a high intensity signal from which the concentration
140 of hydrogen can be determined with high precision and accuracy (Fig. 1c) (Prettyman et al.,
141 2017). This signal was used to map hydrogen on fine spatial scales using data acquired below
142 100-km altitude.

143 Text S1 and S2 describe the data reduction and mapping methods. The ${}^6\text{Li}(n,\alpha)$ reaction
144 rate at each orbital location was determined and corrected for variations in the flux of GCRs
145 using data acquired near the apoapsis of each orbit. Corrections for measurement geometry were
146 made using the forward model described by Prettyman et al. (2017) that accounts for Ceres'
147 overall shape and local topography when the spacecraft was in close proximity to the surface.
148 The corrected counting data were mapped onto the surface using a circle superposition algorithm
149 that accounts for variations in the resolution of the spectrometer with altitude. High-resolution
150 maps are shown in Fig. 2.

151 To validate the sensitivity of the elliptical data to the interior of Occator crater, we
152 averaged the ${}^6\text{Li}(n,\alpha)$ counts for three nearly identical orbits with periapsides near the center of
153 the crater (Fig. S1). The data reveal a significant suppression of counts within the crater and to
154 the south of the crater, consistent with mapped enhancements in hydrogen shown in Fig. 2b.

155 Furthermore, simulations of the response of GRaND to neutrons emitted within geologic units
156 (Fig. S1) supports the sensitivity of the measurements to ice in the lobate deposits and terrace
157 material inside the crater as well as ice in the ejecta blanket.

158 **3 Results**

159 The high spatial resolution maps reveal similar large-scale trends as observed in LAMO
160 (Prettyman et al., 2017) with more hydrogen at high latitudes than near the equator (Figs. 2a, 2b
161 and 3c). This pattern is consistent with the presence of a receding ice table. If the regolith
162 initially contained ice-cemented soil, then the LAMO data can be explained by a low-diffusivity
163 regolith with about 0.2 porosity and 1 μm grain size (Prettyman et al., 2017). In this case, ice is
164 expected to have receded to about 80-90 cm at the equator over Ceres' lifetime. Ice would have
165 been preserved at submillimeter depths poleward of 60 degrees latitude in the northern and
166 southern hemispheres.

167 Forward modeling was used to determine the concentration of hydrogen that would have
168 been observed by GRaND from the eccentric orbit given the distribution of ice that best fits the
169 LAMO data per Prettyman et al. (2017) (green curve in Fig. 2b). The modeled variation in bulk
170 regolith hydrogen approximates the observed variation in the high-resolution data at southern
171 high latitudes. Near the equator (± 30 degrees latitude), the model is nearly constant, indicating
172 ice in this region at depths greater than sensed by GRaND. Within this region, the "best fit"
173 model ice depths from Prettyman et al. (2017) ranged from 50-90 centimeters.

174 In contrast to the model, the high-resolution measurements show variations in hydrogen
175 content with latitude and longitude in the equatorial band. For example, the concentration of
176 hydrogen at low latitudes in eastern and western hemispheres differs by up to 4 wt.% (Fig. 2b).
177 Lower concentrations of hydrogen in the eastern hemisphere are consistent with LAMO
178 observations (Prettyman et al., 2017); however, the high-resolution data reveal small scale
179 variability, including enhanced concentrations of hydrogen in the Occator region (up to 2 wt.%
180 eq. H_2O higher than surroundings). The northern hemisphere has more hydrogen than in the
181 south and hydrogen at high latitudes increases more steeply in the north, perhaps indicating a
182 larger gradient in ice table depth or ice concentration with latitude. The vertical lines that
183 represent the statistical uncertainty in the data (Fig. 2b) indicate these variations are significant.

184 A map of the distribution of hydrogen in the Occator region (Fig. 2c) shows that
185 Occator's interior and portions of the ejecta blanket to the east and south of the crater are richer
186 in hydrogen than the surrounding low latitude region. Geologic mapping shows that Occator's
187 ejecta blanket is asymmetrical, suggesting an oblique impact from the northwest (Scully et al.,
188 2019). Relatively hydrogen-poor materials extend from the northern rim of the crater to the
189 northeast, which partially overlaps a lane of dark ejecta shown in the geologic map (Fig. 2c).
190 Otherwise, the observed distribution of hydrogen is not closely aligned with geologic units.

191 **4 Discussion**

192 Hydrogen within Ceres' regolith is in the form of hydrated minerals, water ice, and other
193 hydrogen-bearing species. Spectral mixing fractions were determined for a suite of detected
194 minerals (Raponi et al., 2019). These included Mg-, Al-, and NH₄-bearing phyllosilicates, Mg-
195 and Na-carbonates, NH₄-chloride, and a darkening agent. Following Marchi et al. (2019), the
196 spectral mixing fractions were interpreted as volume fractions and combined with mineral
197 densities and empirical formulae to estimate the concentration of hydrogen at Occator (Text S3).
198 Both VIR and GRaND maps show a lobe of hydrogen-poor material extending to the northeast
199 from the northern rim of the crater (Fig. 3). Otherwise, they have dissimilar distributions and
200 ranges, most likely due to differences in the hydration state of the regolith layers sensed by the
201 instruments. VIR is sensitive to the uppermost ~100 μm surface layer; whereas, GRaND is
202 sensitive to the uppermost meter. The presence of subsurface ice could account for the
203 comparatively high dynamic range of GRaND data.

204 Outside the faculae, the VIR-derived hydrogen concentration spans 16-17 wt.% eq. H₂O,
205 similar to the lowest values reported by GRaND (Fig. 3a). Natrite (Na₂CO₃) is a significant
206 component of the faculae (Raponi et al., 2019). It was suggested that Na-carbonates were
207 initially hydrated (e.g., Zolotov, 2017); however, these hydrated species are not stable within the
208 shallow subsurface within Occator crater (Text S4). As such, the faculae must be hydrogen poor
209 (estimated to be <10 wt.% eq. H₂O, ignoring bound water) compared to dark background
210 materials. The faculae cover a small portion of the crater floor, well below the spatial scales
211 resolved by GRaND even at closest approach (Fig. S1). Consequently, within the crater hydrated
212 salts are not likely a significant contributor to the hydrogen measured by GRaND.

213 Global variations in regolith hydrogen content, including the observed N-S and E-W
214 differences (Fig. 2), are not likely the result of variations in the concentration of hydrated
215 minerals. The dynamic range of VIR 2.7- and 3.1- μm band depths (OH and NH_4 , respectively) is
216 about one fifth that of subsurface hydrogen on the broad spatial scales sampled by GRaND in
217 LAMO (Ammannito et al., 2016; Prettyman et al., 2019). Some variability in subsurface
218 hydrogen may result from the presence of water bound to salts or interlayer water in clay
219 minerals. Nevertheless, detections of hydrated sodium carbonate are rare (Tosi et al., 2018) and
220 if present may be in a low hydration state as nahcolite (Zolotov, 2017). Hydrated chloride salts,
221 which could represent a significant crustal component depending on the freezing state of the
222 ocean are not likely to be abundant in the shallow subsurface and regolith (Castillo-Rogez et al.,
223 2018). Hydrohalite reported at Cerealia Tholus by De Sanctis et al. (2020) is hypothesized to
224 originate from the deep brine reservoir source of the Occator faculae (Raymond et al., 2020).

225 Relatively high concentrations of hydrogen in the interior of Occator crater and its ejecta
226 blanket likely result from the presence of subsurface water ice. Lobate deposits cover a
227 significant portion ($>30\%$) of the crater floor (Fig. 2c) and may contain high concentrations of
228 water ice (Scully et al., 2019). These likely formed following the impact by mixing of crustal
229 water with rock to produce a water-rich slurry that filled portions of the crater's floor (Raponi et
230 al., 2019; Scully et al., 2019). A portion of the excavated water would have been emplaced in the
231 ejecta blanket (Schröder et al., 2021). The heterogeneous distribution of hydrogen enhancements
232 in and around Occator likely represents variations in the composition of materials ejected by the
233 impact and their thermal history.

234 Thermophysical modeling shows that buried water ice, if present following impact, could
235 still be found at depths sensed by GRaND in both the lobate deposits and the ejecta blanket,
236 given Occator's ~ 20 Myr age (Neesemann et al., 2019) and a plausible range of regolith physical
237 properties (Fig. 3b). Grain sizes determined by VIR in the Occator region are greater than $30 \mu\text{m}$
238 (Raponi et al., 2019), which would result in much higher vapor diffusivity than inferred from
239 GRaND data acquired in LAMO (Prettyman et al., 2017). Consequently, the coarse grain sizes
240 modeled in Fig. 3b provide an upper limit on the expected ice depths.

241 The global N-S asymmetry in hydrogen on Ceres suggests hemispheric differences in
242 regolith ice content. This asymmetry cannot be explained by a receding ice table given Ceres'

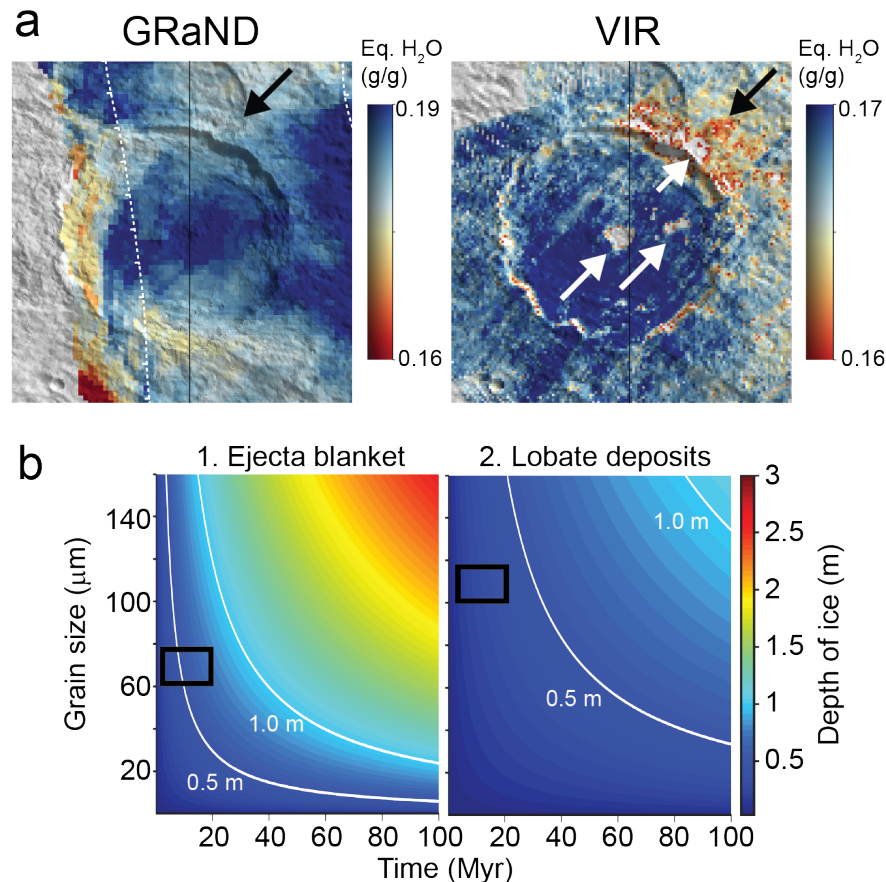
243 precessing orbital elements and reasonable models of surface roughness (Hayne & Aharonson,
244 2015; Landis et al., 2017; Prettyman et al., 2017; Schorghofer, 2016). Nevertheless, the detection
245 of elevated hydrogen concentrations within and around Occator provides evidence for water ice
246 emplaced in the regolith during the formation of large craters. We assess whether this process
247 could influence the global distribution of hydrogen.

248 Hiesinger et al. (2016) catalogued craters greater than 20-diameter. Craters in the 20-100-
249 km range sample the outer ~2- to 10-km of the crust, a layer potentially rich in water ice (Park et
250 al., 2020). The density of these craters when smoothed to the spatial resolution of GRaND
251 exhibits a N-S asymmetry, like hydrogen, with highest density in the northern hemisphere (Fig.
252 4a). In addition, elevated hydrogen concentrations extending from the northern to the southern
253 hemisphere roughly corresponds with craters centered at 180E (Fig. S2). These associations
254 suggest that the global distribution of hydrogen could be controlled – at least in part – by
255 excavation of ice by large impacts; however, this hypothesis cannot fully explain the observed
256 variability in hydrogen concentration (Fig. S3). Impact basins excluded from the crater density
257 map, would have excavated deeper crustal materials perhaps with lower water content,
258 modifying the composition of the regolith and crust in large portions of the eastern and southern
259 hemisphere (e.g., Lawrence et al., 2018). Hidden basins (> 280 km in diameter) would have
260 dominated early regolith production and could also contribute to large-scale variations in the
261 distribution of hydrogen (Marchi et al., 2016).

262 Previous work considered insolation-driven retreat of ice over the 4.5 Gyr lifetime of
263 Ceres (Prettyman et al., 2017). Models predict that modification of the ice table depth by impact
264 gardening is negligible (Costello et al., 2021; Schorghofer, 2016). As such, the GRaND
265 hydrogen data support relatively shallow ice depths (~90 centimeters at the equator), with low
266 inferred regolith vapor diffusivity (effective grain size of 1 μm and 0.2 porosity, Fig. 4b). The
267 presence of μm -size particles is supported by spectrophotometry (Li et al., 2019). This contrasts
268 with 10-100 μm grains derived from infrared observations (Gundlach & Blum, 2013; Raponi et
269 al., 2019). For fixed porosity, vapor diffusivity increases with grain size (Schorghofer, 2016).
270 The ice depths inferred by GRaND can be explained if larger grain sizes are present, but only if
271 the ice was emplaced more recently than 4.5 Gyr. For example, ice deposited ~500 Myr ago
272 would have retreated to 90 centimeters depth at the equator if the grain size were 10 μm .

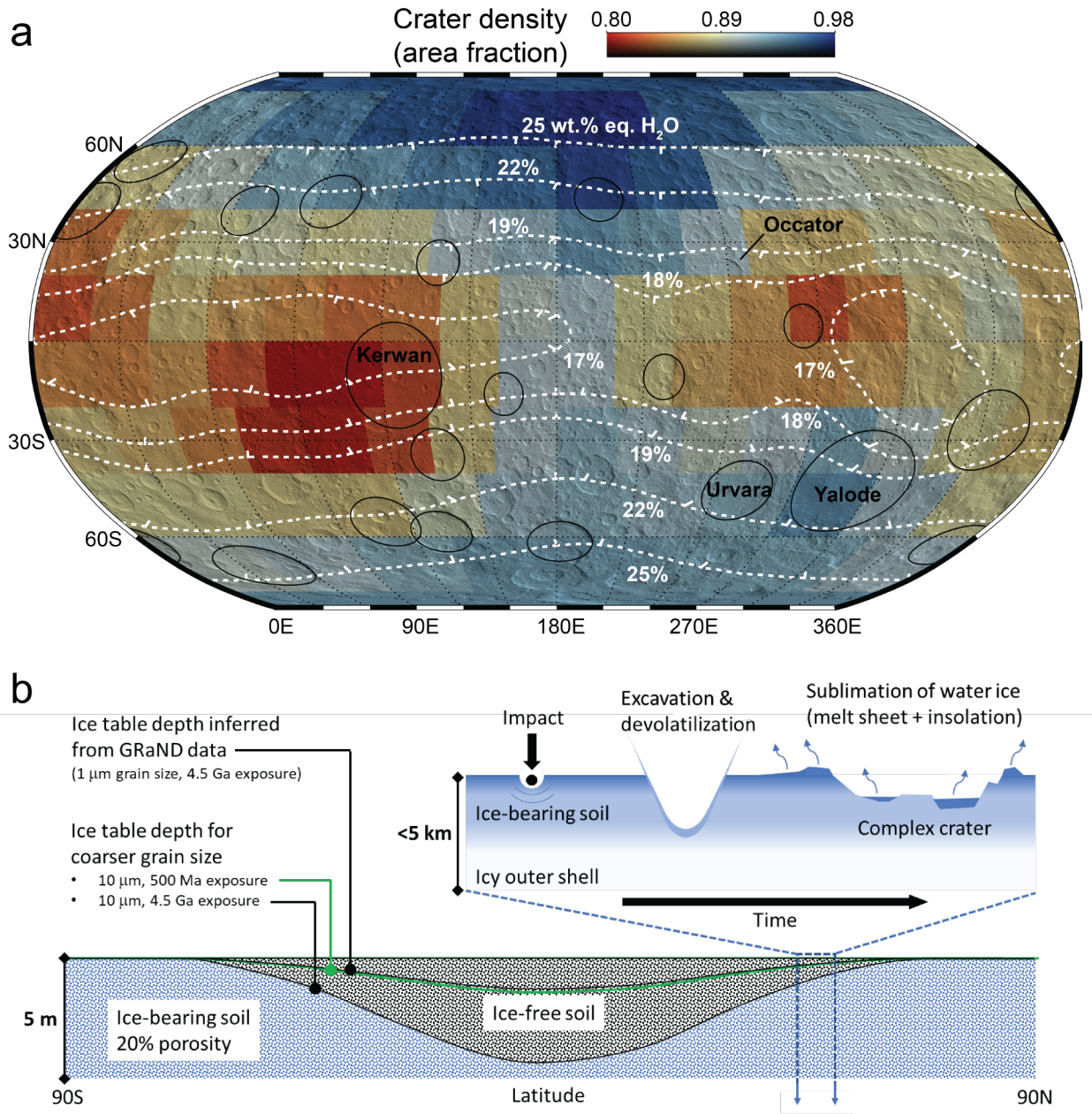
273 Consequently, delivery of crustal ice to the regolith by impacts could influence the depth of near-
 274 surface ice. Assuming granular segregation with depth within the regolith can be ignored, this
 275 could allow reconciliation of GRaND and VIR inferences of grain size.

276



277

278 **Figure 3.** Evidence for water ice at Occator crater. (a) The distribution of hydrogen within and
 279 immediately surrounding Occator determined by GRaND is compared to that inferred from VIR
 280 mineralogy (Text S3) (Marchi et al., 2019; Raponi et al., 2019). The VIR-derived hydrogen
 281 concentration within the facula and portions of the crater rim is <16 wt.% eq. H₂O (white arrows
 282 point to regions with no data in the range indicated by the scalebar). The faculae are smaller than
 283 can be resolved by GRaND. Both maps include a lobe of relatively hydrogen-poor material
 284 extending from the north and east of the crater (black arrows). (b) Thermophysical modeling
 285 shows that ice could survive at depths sensed by GRaND for a range of reported ages
 286 (Neesemann et al., 2019) and feasible regolith thermophysical properties (porosity and grain
 287 size). Two cases are modeled: 1. Impact ejecta emplaced outside the crater are assumed to have
 288 the same porosity (0.2) as determined by GRaND in LAMO. 2. Within the interior of the crater,
 289 ice may have been concentrated in lobate deposits during crater formation (Scully et al., 2019)
 290 (90% water by volume, with an overlying sublimation lag with a porosity of 0.5). Boxes indicate
 291 the most likely range of ages and VIR-derived grain sizes (Raponi et al., 2019).



292

293 **Figure 4.** Impact processes as a partial control on the global distribution of hydrogen. (a) A map
 294 of the density of large craters is compared to the global distribution of hydrogen measured by
 295 GRaND (white contours). The map was determined by smoothing the pattern of large craters
 296 (20- to 100-km diameter) catalogued by Hiesinger et al. (2016) to the spatial resolution of
 297 GRaND in LAMO using the smoothing algorithm of Prettyman et al. (2019). A density of 1
 298 indicates craters fully cover the surface within GRaND's field of view. For context, the map is
 299 superimposed on shaded relief and excluded basins with diameters greater than 100 km are
 300 outlined (black). Associations between crater density and the global distribution of hydrogen are
 301 detailed in Figs. S2 and S3. (b) A possible scenario for enrichment of surficial ice by large
 302 impacts is illustrated. A portion of the ice excavated from the crust survives during crater
 303 formation and cooling of the melt sheet and ejecta blanket, enriching the regolith in water ice.
 304 The surviving ice retreats in response to solar insolation.

305 **5 Conclusions**

306 Our analysis suggests the distribution of water ice within Ceres' bulk regolith is
307 controlled by a combination of insolation-driven sublimation and delivery of water-bearing
308 materials to the regolith from the volatile-rich outer crust by large impacts. The observed
309 enrichment in hydrogen within Occator crater and ejecta blanket shows that excavated ice not
310 only survives large impacts but also enhances the concentration of ice in the shallow subsurface.
311 Associations between the pattern of large craters and the distribution of hydrogen suggest this
312 process could be pervasive on Ceres. Impact replenishment of the regolith with crustal ice would
313 allow the GRaND data to be explained by younger surface ages with larger regolith grain sizes
314 more consistent with those inferred from infrared spectroscopy.

315 The high-resolution GRaND data support an endogenic crustal origin for ice within the
316 regolith. Since the excavation depth of Occator was nearly 10 km, our results bring direct
317 evidence for a large amount of ice in Ceres' crust, consistent with indirect inferences from
318 geological observations (e.g., Sizemore et al., 2019). Alternative interpretations of the Dawn
319 geophysical data in terms of an ice-free Ceres (Zolotov, 2020) are thus inconsistent with the
320 GRaND data. The results also support the recent interpretation proposed by Schröder et al.
321 (2021) for the distinctly blue color of ejecta from recent impact craters as an evolved mixture of
322 ice and minerals.

323 **Acknowledgments**

324 Funding was provided by the NASA Discovery Data Analysis Program, the NASA
325 SSERVI Toolkit for Research and Exploration project, and the NASA Dawn Mission. Part of
326 this work was carried out at the Jet Propulsion Laboratory, California Institute of Technology,
327 under contract to NASA. We thank B. L. Ehlmann for contributions to the interpretation of the
328 data. The Dawn Flight Team acquired the special, high-resolution data set used in this study. The
329 GRaND data are available from the NASA Planetary Data System at
330 <https://sbn.psi.edu/pds/resource/dawn/dawngrandPDS4.html>.

References

- Ammannito, E., DeSanctis, M. C., Ciarniello, M., Frigeri, A., Carrozzo, F. G., Combe, J.-P., et al. (2016). Distribution of phyllosilicates on the surface of Ceres. *Science*, *353*(6303), aaf4279. doi:10.1126/science.aaf4279
- Bu, C., Rodriguez Lopez, G., Dukes, C. A., McFadden, L. A., Li, J. Y., & Ruesch, O. (2018a). Stability of hydrated carbonates on Ceres. *Icarus*, *320*, 136-149. doi:<https://doi.org/10.1016/j.icarus.2017.12.036>
- Bu, C., Rodriguez Lopez, G., Dukes, C. A., Ruesch, O., McFadden, L. A., & Li, J. Y. (2018b). Search for sulfates on the surface of Ceres. *Meteoritics & Planetary Science*, *53*(9), 1946-1960. doi:10.1111/maps.13024
- Carrozzo, F. G., De Sanctis, M. C., Raponi, A., Ammannito, E., Castillo-Rogez, J., Ehlmann, B. L., et al. (2018). Nature, formation, and distribution of carbonates on Ceres. *Science Advances*, *4*(3), e1701645. doi:10.1126/sciadv.1701645
- Castillo-Rogez, J., Neveu, M., McSween, H. Y., Fu, R. R., Toplis, M. J., & Prettyman, T. (2018). Insights into Ceres's evolution from surface composition. *Meteoritics & Planetary Science*, *53*(9), 1820-1843. doi:10.1111/maps.13181
- Combe, J.-P., Raponi, A., Tosi, F., De Sanctis, M. C., Carrozzo, F. G., Zambon, F., et al. (2019). Exposed H₂O-rich areas detected on Ceres with the dawn visible and infrared mapping spectrometer. *Icarus*, *318*, 22-41. doi:10.1016/j.icarus.2017.12.008
- Costello, E. S., Ghent, R. R., & Lucey, P. G. (2021). Impact Gardening on Ceres. *Geophysical Research Letters*, *n/a*(n/a), e2021GL092960. <https://doi.org/10.1029/2021GL092960>. doi:<https://doi.org/10.1029/2021GL092960>
- De Sanctis, M. C., Ammannito, E., Raponi, A., Marchi, S., McCord, T. B., McSween, H. Y., et al. (2015). Ammoniated phyllosilicates with a likely outer Solar System origin on (1) Ceres. *Nature*, *528*(7581), 241-244. doi:10.1038/nature16172
- De Sanctis, M. C., Ammannito, E., Raponi, A., Frigeri, A., Ferrari, M., Carrozzo, F. G., et al. (2020). Fresh emplacement of hydrated sodium chloride on Ceres from ascending salty fluids. *Nature Astronomy*, *4*(8), 786-793. doi:10.1038/s41550-020-1138-8
- Ermakov, A. I., Fu, R. R., Castillo-Rogez, J. C., Raymond, C. A., Park, R. S., Preusker, F., et al. (2017). Constraints on Ceres' internal structure and evolution from its shape and gravity measured by the Dawn spacecraft. *Journal of Geophysical Research: Planets*, *122*(11), 2267-2293. doi:10.1002/2017je005302
- Fu, R. R., Ermakov, A. I., Marchi, S., Castillo-Rogez, J. C., Raymond, C. A., Hager, B. H., et al. (2017). The interior structure of Ceres as revealed by surface topography. *Earth and Planetary Science Letters*, *476*, 153-164. doi:10.1016/j.epsl.2017.07.053
- Gundlach, B., & Blum, J. (2013). A new method to determine the grain size of planetary regolith. *Icarus*, *223*(1), 479-492. doi:<https://doi.org/10.1016/j.icarus.2012.11.039>
- Haines, E. L., Etchegaray-Ramirez, M. I., & Metzger, A. E. (1978). Thorium concentrations in the lunar surface. II: Deconvolution modeling and its application to the regions of Aristarchus and Mare Smythii. *Proc. Lunar Planet. Sci. Conf. 9th*, 2985-3013.

- Hayne, P. O., & Aharonson, O. (2015). Thermal stability of ice on Ceres with rough topography. *Journal of Geophysical Research: Planets*, *120*(9), 1567-1584. doi:10.1002/2015je004887
- Hiesinger, H., Marchi, S., Schmedemann, N., Schenk, P., Pasckert, J. H., Neesemann, A., et al. (2016). Cratering on Ceres: Implications for its crust and evolution. *Science*, *353*(6303), aaf4759. doi:10.1126/science.aaf4759
- Landis, M. E., Byrne, S., Schörghofer, N., Schmidt, B. E., Hayne, P. O., Castillo-Rogez, J., et al. (2017). Conditions for sublimating water ice to supply Ceres' exosphere. *Journal of Geophysical Research: Planets*, *122*(10), 1984-1995. doi:10.1002/2017JE005335
- Landis, M. E., Byrne, S., Combe, J.-P., Marchi, S., Castillo-Rogez, J., Sizemore, H. G., et al. (2019). Water vapor contribution to Ceres' exosphere from observed surface ice and postulated ice-exposing impacts. *Journal of Geophysical Research: Planets*, *124*(1), 61-75. doi:10.1029/2018je005780
- Lawrence, D., Elphic, R., Feldman, W., Prettyman, T., Gasnault, O., & Maurice, S. (2003). Small-area thorium features on the lunar surface. *Journal of Geophysical Research*, *108*(E9), 5102.
- Lawrence, D. J., Peplowski, P. N., Beck, A. W., Feldman, W. C., Prettyman, T. H., Russell, C. T., et al. (2018). Compositional variability on the surface of 1 Ceres revealed through GRaND measurements of high-energy gamma rays. *53*(9), 1805-1819. doi:10.1111/maps.13124
- Li, J.-Y., Reddy, V., Nathues, A., Corre, L. L., Izawa, M. R. M., Cloutis, E. A., et al. (2016). Surface albedo and spectral variability of Ceres. *The Astrophysical Journal*, *817*(2), L22. doi:10.3847/2041-8205/817/2/L22
- Li, J.-Y., Schröder, S. E., Mottola, S., Nathues, A., Castillo-Rogez, J. C., Schorghofer, N., et al. (2019). Spectrophotometric modeling and mapping of Ceres. *Icarus*, *322*, 144-167. doi:<https://doi.org/10.1016/j.icarus.2018.12.038>
- Marchi, S., Ermakov, A. I., Raymond, C. A., Fu, R. R., O'Brien, D. P., Bland, M. T., et al. (2016). The missing large impact craters on Ceres. *Nature Communications*, *7*, 12257. Article. doi:10.1038/ncomms12257
- Marchi, S., Raponi, A., Prettyman, T. H., De Sanctis, M. C., Castillo-Rogez, J., Raymond, C. A., et al. (2019). An aqueously altered carbon-rich Ceres. *Nature Astronomy*, *3*(2), 140-145. doi:10.1038/s41550-018-0656-0
- Maurice, S., Lawrence, D. J., Feldman, W. C., Elphic, R. C., & Gasnault, O. (2004). Reduction of neutron data from Lunar Prospector. *Journal of Geophysical Research: Planets*, *109*(E7). doi:10.1029/2003JE002208
- McCord, T. B., Orlando, T. M., Teeter, G., Hansen, G. B., Sieger, M. T., Petrik, N. G., & Van Keulen, L. (2001). Thermal and radiation stability of the hydrated salt minerals epsomite, mirabilite, and natron under Europa environmental conditions. *Journal of Geophysical Research*, *106*(E2), 3311-3319. doi:10.1029/2000JE001282
- McKinney, G. W., Lawrence, D. J., Prettyman, T. H., Elphic, R. C., Feldman, W. C., & Hagerty, J. J. (2006). MCNPX benchmark for cosmic ray interactions with the Moon. *Journal of Geophysical Research*, *111*(E6), E06004. doi:10.1029/2005je002551
- McSween, H. Y., Emery, J. P., Rivkin, A. S., Toplis, M. J., C. Castillo-Rogez, J., Prettyman, T. H., et al. (2017). Carbonaceous chondrites as analogs for the composition and alteration of Ceres. *Meteoritics & Planetary Science*, *53*(8), 1793-1804. doi:10.1111/maps.12947

- Neesemann, A., van Gasselt, S., Schmedemann, N., Marchi, S., Walter, S. H. G., Preusker, F., et al. (2019). The various ages of Occator crater, Ceres: Results of a comprehensive synthesis approach. *Icarus*, *320*, 60-82. doi:10.1016/j.icarus.2018.09.006
- Park, R. S., & Buccino, D. R. (2018). Ceres SPC Shape Model Dataset V1.0, DAWN-A-FC2-5-CERESSHAPESPC-V1.0. *NASA Planetary Data System*.
- Park, R. S., Vaughan, A. T., Konopliv, A. S., Ermakov, A. I., Mastrodemos, N., Castillo-Rogez, J. C., et al. (2019). High-resolution shape model of Ceres from stereophotoclinometry using Dawn Imaging Data. *Icarus*, *319*, 812-827. doi:10.1016/j.icarus.2018.10.024
- Park, R. S., Konopliv, A. S., Ermakov, A. I., Castillo-Rogez, J. C., Fu, R. R., Hughson, K. H. G., et al. (2020). Evidence of non-uniform crust of Ceres from Dawn's high-resolution gravity data. *Nature Astronomy*, *4*(8), 748-755. doi:10.1038/s41550-020-1019-1
- Prettyman, T. H., Feldman, W. C., & Titus, T. N. (2009). Characterization of Mars' seasonal caps using neutron spectroscopy. *Journal of Geophysical Research*, *114*(E8). doi:10.1029/2008je003275
- Prettyman, T. H., Feldman, W. C., McSween, H. Y., Jr., Dingler, R. D., Enemark, D. C., Patrick, D. E., et al. (2011). Dawn's gamma ray and neutron detector. *Space Science Reviews*, *163*(1), 371-459. doi:10.1007/s11214-011-9862-0
- Prettyman, T. H., Mittlefehldt, D. W., Yamashita, N., Lawrence, D. J., Beck, A. W., Feldman, W. C., et al. (2012). Elemental mapping by Dawn reveals exogenic H in Vesta's regolith. *Science*, *338*(6104), 242-246. doi:10.1126/science.1225354
- Prettyman, T. H., Yamashita, N., Toplis, M. J., McSween, H. Y., Schorghofer, N., Marchi, S., et al. (2017). Extensive water ice within Ceres' aqueously altered regolith: Evidence from nuclear spectroscopy. *Science*, *355*(6320), 55-59. doi:10.1126/science.aah6765
- Prettyman, T. H., Yamashita, N., Ammannito, E., Ehlmann, B. L., McSween, H. Y., Mittlefehldt, D. W., et al. (2019). Elemental composition and mineralogy of Vesta and Ceres: Distribution and origins of hydrogen-bearing species. *Icarus*, *318*, 42-55. doi:10.1016/j.icarus.2018.04.032
- Quick, L. C., Buczkowski, D. L., Ruesch, O., Scully, J. E. C., Castillo-Rogez, J., Raymond, C. A., et al. (2019). A possible brine reservoir beneath Occator Crater: Thermal and compositional evolution and formation of the Cerealia dome and Vinalia Faculae. *Icarus*, *320*, 119-135. doi:10.1016/j.icarus.2018.07.016
- Raponi, A., De Sanctis, M. C., Carrozzo, F. G., Ciarniello, M., Castillo-Rogez, J. C., Ammannito, E., et al. (2019). Mineralogy of Occator crater on Ceres and insight into its evolution from the properties of carbonates, phyllosilicates, and chlorides. *Icarus*, *320*, 83-96. doi:10.1016/j.icarus.2018.02.001
- Raymond, C. A., Ermakov, A. I., Castillo-Rogez, J. C., Marchi, S., Johnson, B. C., Hesse, M. A., et al. (2020). Impact-driven mobilization of deep crustal brines on dwarf planet Ceres. *Nature Astronomy*, *4*(8), 741-747. doi:10.1038/s41550-020-1168-2
- Rivkin, A. S., Li, J.-Y., Milliken, R. E., Lim, L. F., Lovell, A. J., Schmidt, B. E., et al. (2011). The Surface Composition of Ceres. In C. Russell & C. Raymond (Eds.), *The Dawn Mission to Minor Planets 4 Vesta and 1 Ceres* (pp. 95-116). New York, NY: Springer New York.
- Ruesch, O., Genova, A., Neumann, W., Quick, L. C., Castillo-Rogez, J. C., Raymond, C. A., et al. (2019). Slurry extrusion on Ceres from a convective mud-bearing mantle. *Nature Geoscience*, *12*(7), 505-509. doi:10.1038/s41561-019-0378-7

- Russell, C. T., Raymond, C. A., Ammannito, E., Buczkowski, D. L., De Sanctis, M. C., Hiesinger, H., et al. (2016). Dawn arrives at Ceres: Exploration of a small, volatile-rich world. *Science*, 353(6303), 1008-1010. doi:10.1126/science.aaf4219
- Schenk, P., Castillo-Rogez, J., Otto, K. A., Marchi, S., O'Brien, D., Bland, M., et al. (2021). Compositional control on impact crater formation on mid-sized planetary bodies: Dawn at Ceres and Vesta, Cassini at Saturn. *Icarus*, 359, 114343. doi:<https://doi.org/10.1016/j.icarus.2021.114343>
- Schorghofer, N. (2008). The lifetime of ice on main belt asteroids. *Astrophysical Journal*, 682(1), 697-705. doi:10.1086/588633
- Schorghofer, N. (2016). Predictions of depth-to-ice on asteroids based on an asynchronous model of temperature, impact stirring, and ice loss. *Icarus*, 276, 88-95. doi:10.1016/j.icarus.2016.04.037
- Schröder, S. E., Poch, O., Ferrari, M., Angelis, S. D., Sultana, R., Potin, S. M., et al. (2021). Dwarf planet (1) Ceres surface bluing due to high porosity resulting from sublimation. *Nature Communications*, 12(1), 274. doi:10.1038/s41467-020-20494-5
- Scully, J. E. C., Buczkowski, D. L., Raymond, C. A., Bowling, T., Williams, D. A., Neesemann, A., et al. (2019). Ceres' Occator crater and its faculae explored through geologic mapping. *Icarus*, 320, 7-23. doi:10.1016/j.icarus.2018.04.014
- Sizemore, H. G., Platz, T., Schorghofer, N., Prettyman, T. H., De Sanctis, M. C., Crown, D. A., et al. (2017). Pitted terrains on (1) Ceres and implications for shallow subsurface volatile distribution. *Geophys Res Lett*, 44(13), 6570-6578. doi:10.1002/2017GL073970
- Sizemore, H. G., Schmidt, B. E., Buczkowski, D. A., Sori, M. M., Castillo-Rogez, J. C., Berman, D. C., et al. (2019). A Global Inventory of Ice-Related Morphological Features on Dwarf Planet Ceres: Implications for the evolution and current state of the cryosphere. *Journal of Geophysical Research: Planets*. doi:10.1029/2018JE005699
- Tosi, F., Carrozzo, F. G., Raponi, A., De Sanctis, M. C., Thangjam, G., Zambon, F., et al. (2018). Mineralogy and temperature of crater Haulani on Ceres. *Meteoritics & Planetary Science*, 53(9), 1902-1924. <https://doi.org/10.1111/maps.13078>. doi:<https://doi.org/10.1111/maps.13078>
- Williams, D. A., Buczkowski, D. L., Mest, S. C., Scully, J. E. C., Platz, T., & Kneissl, T. (2018). Introduction: The geologic mapping of Ceres. *Icarus*, 316, 1-13. doi:<https://doi.org/10.1016/j.icarus.2017.05.004>
- Williams, D. A., Buczkowski, D. L., Crown, D. A., Frigeri, A., Hughson, K., Kneissl, T., et al. (2019). Final Dawn LAMO-based global geologic map of Ceres. *Lunar and Planetary Science Conference, L*, Abstract #1252.
- Zolotov, M. Y. (2017). Aqueous origins of bright salt deposits on Ceres. *Icarus*, 296, 289-304. doi:10.1016/j.icarus.2017.06.018
- Zolotov, M. Y. (2020). The composition and structure of Ceres' interior. *Icarus*, 335, 113404. doi:<https://doi.org/10.1016/j.icarus.2019.113404>